ELSEVIER

Contents lists available at ScienceDirect

Surface & Coatings Technology

journal homepage: www.elsevier.com/locate/surfcoat





The microstructural and stress evolution in sputter deposited Ni thin films

Thomas R. Koenig a, Zhaoxia Rao b, Eric Chason b, Garritt J. Tucker c, Gregory B. Thompson a,*

- ^a University of Alabama, Department of Metallurgical & Materials Engineering, Tuscaloosa, AL 35401, United States of America
- b Brown University, School of Engineering, Providence, RI 02912, United States of America
- ^c Colorado School of Mines, Department of Mechanical Engineering, Golden, CO 80401, United States of America

ARTICLEINFO

Keywords: Thin film Intrinsic stress Sputter deposition Microstructure Transmission electron microscopy Precession electron diffraction Nickel

ABSTRACT

We report the stress and microstructural evolution for a series of Ni thin films sputter deposited over a range of rates (0.076 and 0.250 nm/s), pressures (0.27, 0.67 and 1.33 Pa), and substrate temperatures (ambient, 100, and 200 °C). In general, as the sputtering pressure increased, the stress-thickness product, measured by wafer curvature, became tensile and trended with an increase in pressure regardless of the deposition rate. However, at the lowest sputtering rate and highest substrate temperature, the films exhibited a compressive growth stress. The collective data was then fitted to a kinetic model that accounts for the stress generation at the grain boundaries, from grain growth, and from the creation of defects within the film. The model's predicted fitted parameters matched well to the experimental measurements except for films deposited at the lowest deposition pressure. These particular films exhibited a bimodal grain size distribution which could not be accommodated by the model's use of a singular grain diameter. Nevertheless, in monomodal grain sizes, the results do provide support for the kinetic model in helping to ascertain the various contributing factors for the intrinsic stress development and their microstructural relationship in context to the Thornton zonal morphology descriptors for thin films and coatings.

1. Introduction

It is well known that the macroscopic properties, such as hardness, thermal and electrical transport, and optical descriptors of materials are linked to their microstructural characteristics. Through variation of processing parameters, microstructures can be altered enabling these properties to be controlled. In the case of thin film deposits, microstructural characteristics such as grain size and their grain morphology can vary widely between and within deposition techniques, resulting in a variation of the physical responses noted above, even for the same material [1-3]. In particular to thin films, they may retain significant internal residual stresses as a result of the deposition process which then influences those particular properties [4,5]. These stresses can also lead to film failure by buckling, cracking, or delamination mechanisms [6,7]. Indeed, when considering the properties of a film, both the material microstructure and its residual stress characteristics must be concurrently quantified. Understanding the relationship between the deposited microstructure and its residual stress is a clear prerequisite for tailoring thin film properties.

While residual stress has been an area of research for over 100 years

[8], unraveling the mechanisms, with associated models, has significantly advanced in the last two decades giving more clarity on the origins of such stresses [9-13]. The development of in situ measurement techniques [14-16], in conjunction with post-deposition characterization methods, have been critical in elucidating these fundamental mechanisms. For example, polycrystalline films deposited through conventional low-energy deposition techniques exhibit a characteristic stress evolution response dependent on the relationship between the mobility of the deposited species, the rate of deposition, and the substrate temperature [17]. The interaction between these processing parameters can yield a wide range of residual stresses from highly compressive to highly tensile [3,18] even for the same type of film using the same deposition technique. For example, electrodeposited Ni films demonstrate a range of stresses from compressive, \approx - 60 MPa, to tensile, 400 MPa [18], while electron-beam evaporated Ni films exhibit similar residual stress ranges from §0-MPa to 333 MPa [2].

It is generally agreed that tensile stresses evolve as the film coalesces together as the initial islands 'stretch' towards each other to eliminate their free surfaces and associated interfacial energy [2,10,19]. Upon coalescence, the stress can either continue to retain a tensile stress,

E-mail address: gthompson@eng.ua.edu (G.B. Thompson).

^{*} Corresponding author.

which is attributed to low adatom mobility over the coalesced surface or become compressive. The compressive stress generation mechanism has been proposed to include capillary effects [9], surface stresses generated by adatoms [13], inheritance effects of the pre-coalescence stress behavior [20], the incorporation of adatoms onto film ledges [10], highenergy atoms providing an 'atom (shot) peening' effect [21], and/or the motion of adatoms into the grain boundaries themselves [11]. Though several studies have reported stress responses, there are far fewer holistic investigations where sufficient parametric control has been undertaken to monitor the stress such that those results can be directly tied to models that account for the stress evolution mechanism(s) [2,22,23]. This paper reports such a controlled series of experiments for the sputter deposition of Ni, which has a strong technical interest for its use in integrated circuits and memory devices [24-26]. Furthermore, the work expands upon the applicability of the model compared to prior works. For example in reference [22], a thin seed layer of Cu was deposited to inhibit grain growth through the thickness of the film, reducing the parameters for the kinetic model to fit. However, in this work we allow the grain size to grow during film growth, providing a more complex case for the model to fit.

This works adds to the body of literature for Ni deposition, such as those studies previously noted for electron-beam evaporation and electrodeposition where a range of stress states and values are noted. In particular to the electron-beam study [2], key findings include a tensile stress growth state as well as grain growth during deposition, with such growth contributing to the reported stress evolution. But, unlike either electron-beam or electrodeposition, sputter deposition is considered a highly energetic process where additional contributions, including energetic-based grain boundary densification and defect formations, occur and must be accounted for in the stress evolution. By changing the various sputtering parameters of rate, pressure and substrate temperature, one can ascertain their particular contributions. Furthermore, a corresponding evolution in the film microstructure will be concurrent to these process changes, as already noted in the other deposition techniques of Ni. with such changes intimately linked to the stress-state [2,27].

Microstructures in sputter deposited films are often classically described by the qualitative Thornton zonal model [20,28]. In this model the grain morphology is divided into 'zones' based upon the sputtering pressure and homologous temperature during deposition. Though prior efforts have been undertaken to investigate these microstructural characteristics of sputter deposited Ni [29–31], no studies have extensively yet linked the microstructural characteristics of the deposits to their stress-thickness behavior. In this work, we expand the processing window to now include the energetic deposition from sputter deposition such that we can model the stress responses using a kinetic model [32]. In doing so we are able to ascertain the contribution(s) associated with the energetic aspects of sputtering while simultaneously tying the stress-thickness response to microstructural characteristics.

2. Material and methods

The Ni films were deposited via balanced magnetron sputtering in an AJA ATC-1500 sputtering chamber equipped with four con-focal targets and an AJA SHQ 2002-2L heater controller. To maintain uniform deposition rates, each film was deposited from either a single Ni target at lower pressures or co-sputtered at higher pressures using multiple Ni targets, with each target having a purity >99.99%. All films were deposited onto a Si $(100\,$ substrate with a 100 nm thermally grown surface oxide layer rotated at 30 rotations per minute. Prior to sputtering, the base pressure was $<4.0\times 10^{-6}\,\mathrm{Pa}$, wherein ultra-high purity Ar was flowed into the chamber at a rate of 15 standard cubic centimeters per minute while a gate valve adjusted the pumping rate to achieve the working gas pressures of either 0.267 Pa, 0.667 Pa, or 1.33 Pa. Achieving the lowest base pressure as well as ensuring the purity of the working gas was done to reduce potential spurious contaminate

effects, such as oxygen, on the stress evolution of the growing film. Under each working pressure condition, depositions were made at rates of 0.076 nm/s or 0.250 nm/s with the growth rates measured in situ at each pressure condition through a quartz crystal microbalance that was calibrated by post-deposition transmission electron microscopy measurements of the film's cross sectional thickness. The films were deposited to a thickness of approximately 200 nm. Under these conditions, the Thornton model [20] predicts those films deposited at 0.267 Pa and 0.667 Pa to exhibit a Zone T microstructure which is described as a transition structure consisting of densely packed fibrous grains that exhibit a V-shaped 'blossoming' of those grains from the substrate in the cross-sectional view. The films deposited at 1.33 Pa are predicted to lie within the Zone 1 regime, which is generally described as porous structures consisting of tapered crystallites separated by voids. Though these zones are described with distinct microstructural features, the processing dependent conditions for their growth morphologies should only be considered general guidelines and should not be taken as absolute.

In addition to the ambient depositions, which is taken as 20 °C, an additional sub-set of films were deposited at elevated temperatures of 100 °C or 200 °C at a working pressure of 0.667 Pa while maintaining the aforementioned deposition rates to study thermal effects on the thin film microstructure and stress evolution. The substrate temperature set point was measured using a k-Space Associates® BANDIT device that measures the absorption edge of Si as a function of temperature. The substrate set points were calibrated to measurements previously performed on calibration Si wafers. Each substrate was heated to the deposition temperature required for at least 1 h prior to deposition to ensure thermal equilibrium and allowed to cool after deposition for at least 4 h prior to removal from the vacuum chamber to prevent oxidation. The effect of substrate heating from the sputtering targets themselves is considered negligible in this work because of the far cathode-tosubstrate distance of nearly 16 cm. These depositions, onto a heated substrate, are predicted to maintain the Zone T or Zone 1 microstructure above and would increase the adatom mobility without significant change in microstructure [20].

All internal stress values were measured in situ through the k-Space Associates® multibeam optical sensor system (MOS). The system passes a laser through a series of etalons which generate an array of spots that reflect off the surface of the substrate and are captured on a charge couple device (CCD) camera. As the film deposits onto the substrate, the substrate bends in response to the mechanical stress with its radius of curvature dependent upon the magnitude of the stress. The substrate curvature shifts the reflected laser spot positions. Using the Stoney equation [33,34], Eq. (1), the average stress in the thin film is quantified.

$$\overline{\sigma} = \frac{\kappa M_s h^2}{6h_t^s} \tag{1}$$

wherein M_s is the biaxial modulus of the substrate, h_s and h_f are the substrate (250 μ m) and film thicknesses, respectively, and κ is the measured curvature. The product σh_f is proportional to the wafer curvature and is referred to as the stress-thickness product.

Samples were microstructurally characterized through the plane normal, hereafter referred to as plan-view, and through the film cross-section. The plan-view samples were prepared by cutting 3 mm diameter discs, ground down to $<\!100~\mu m$ thickness, dimpled to a thickness of $<\!10~\mu m$ with a Fischione model 200 dimple grinder from the substrate side, and ion milled using a Gatan Precision Ion Polishing System until perforation holes were created, with the regions around the holes being electron transparent, i.e. less than 200 nm thick. The cross sectional samples were prepared using a focus ion beam (FIB) milling lift-out technique [35] using an FEI Quanta 200 Dual-Beam Scanning Electron Microscope (SEM) - FIB. Scanning transmission electron microscopy (STEM) analysis was conducted in a 200 keV FEI Tecnai G^2 Supertwin

TEM. Orientation mapping of the specimens in the plan-view was conducted using the Nanomegas ASTAR PED system within the TEM at a precession angle of 0.3° and a step size of 3 nm. Automatic Crystallographic Orientation Mapping (ACOM) from the identified diffraction patterns was completed through OIM Analysis v7. A multi-iterative grain dilation procedure with a minimum grain size of 5 nm and a minimum tolerance angle of 5° clean-up was applied to each data set processed. All calculations were made with a minimum confidence index of 0.10.

For the kinetic modeling, a MatLab® code was developed to determine the model parameters from the non-linear least-squares fitting to the measured stress-thickness curves. The specific features of the model are developed later in the paper. Some of the deposition conditionindependent parameters were made to be common across all the data sets while other parameters expected to vary between deposits were allowed to be changed independently. This fitting procedure will be further elaborated upon in the discussion section. This approach yielded the best possible fits to the experimentally gathered stress-thickness data. The fitting parameters were then compared to prior nonenergetic terms for Ni deposition [32] to determine if the values are reasonable and give confidence to the fit. Furthermore, the calculated final grain sizes predicted from the model were compared to the experimentally measured final grain sizes to further ascertain the accuracy of the fitted parameters of the model. Note that the grain sizes are reported from plan-view PED grain size distributions reconstructed via OIM v7.

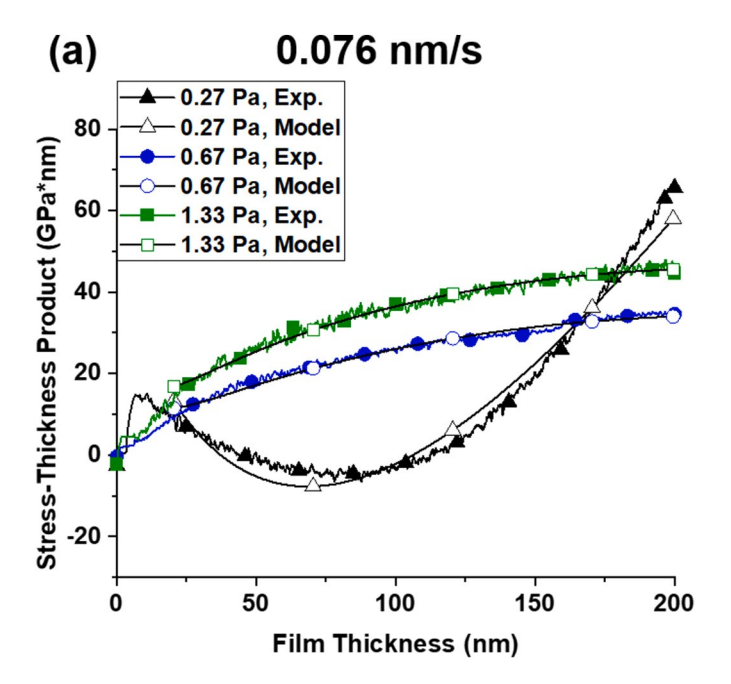
3. Results and discussion

3.1. Ambient temperature deposits

Ambient temperature in situ stress-thickness measurements at different pressures and growth rates are displayed in Fig. 1, along with the results obtained from the fitting. For the working pressures of 0.67 Pa and 1.33 Pa, the film retained a tensile behavior throughout the deposition and the magnitude of the tensile stress increased as the deposition rate increased. At the lower pressure deposition condition of 0.27 Pa, an initial tensile stress is observed for both deposition rates which is attributed to island coalescence before the compressive mechanisms dominated the growth behavior. Following the tensile peak, the stress-thickness slope (referred to as the incremental stress) is negative, indicating that the new layers that are growing are doing so in a compressive state. The magnitude of the incremental compressive stress is observed to increase slightly as the deposition rate is increased from 0.076 nm/s, Fig. 1(a), to 0.250 nm/s, Fig. 1(b), which is seen in other sputtered films in the compressive regime [22,36]. At larger thicknesses, a minimum is observed, and the subsequent positive slope corresponds to a tensile incremental stress.

The dependence on the deposition pressure can be explained in terms of the change in the kinetic energy of the arriving species through increasing the number of collisions between the target and substrate. Increasing the deposition pressure reduces the arrival energy of the sputtered Ni species from 10.4 eV at 0.27 Pa to 1.03 eV at 1.33 Pa according to SIMTRA calculations (for input parameters, see Appendix A, Table A1. The reduction in the arrival kinetic energy can then result in more tensile stress for several reasons. A lower kinetic energy reduces the mobility of the adatoms on the surface; therefore, the migration ability of such adatoms limits their contribution to the compressive stress generation mechanisms in the post-coalescence deposition regime. It also reduces the collision-induced grain boundary densification and trapping of particle-induced defects that can lead to compressive stress [23].

The stress-thickness product is not linear with thickness for all ambient temperature deposits in Fig. 1. This suggests that grain growth occurs during the deposition process itself [32]. The grain size evolution was quantified in post-mortem STEM images in cross-section, Fig. 2.



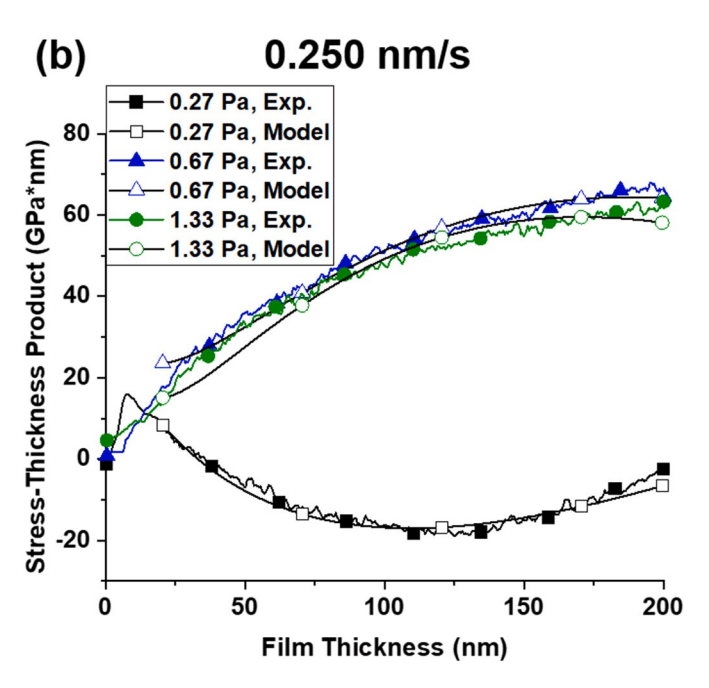


Fig. 1. Calculated and experimental stress-thickness curves for Ni deposited at ambient temperature (20 $^{\circ}$ C) with deposition rates of **(a)** 0.076 nm/s and **(b)** 0.250 nm/s. Modeled fits to the experimental curves correlate notably better at 0.67 Pa and 1.33 Pa.

These micrographs additionally suggest significant differences in the film growth kinetics as equiaxed (0.27 Pa -0.076 nm/s; 0.27 Pa -0.250 nm/s) and columnar (0.67 Pa -0.076 nm/s; 0.67 Pa -0.250 nm/s; 1.33 Pa -0.076 nm/s; 0.67 Pa -0.250 nm/s) morphologies were present and generally follow the Thornton zonal microstructure model [20]. The STEM micrographs, Fig. 2(b,c,e,f), reveal that the films are not fully densified at 0.67 Pa and 1.33 Pa, evident by the darker lines in the images where no signal is detected. In addition, the films deposited at 0.27 Pa reveal drastically different growth kinetics in this cross-sectional view, Fig. 2(a,d), which results in clear microstructural differences as compared to only being evaluated in the plan-view orientation, Fig. 3. Notably, the films deposited at 0.27 Pa, Fig. 2(a,d) are significantly smoother at the surface of the film as compared to those films deposited

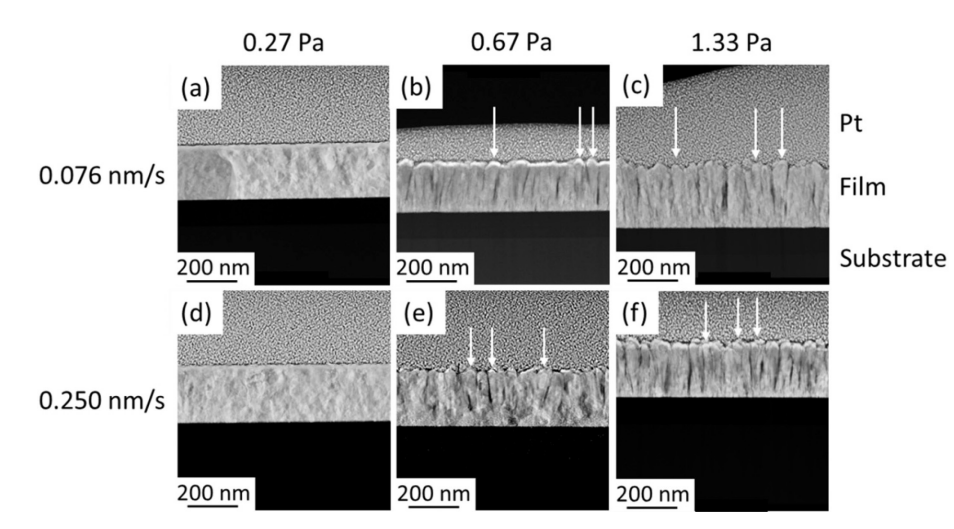


Fig. 2. STEM micrographs of the ambient deposited Ni films in cross-section **(a)** 0.27 Pa / 0.076 nm/s in which small equiaxed grains are observed; **(b)** 0.67 Pa / 0.076 nm/s in which grains exhibit zone T growth with fissures between the grains; **(c)** 1.33 Pa / 0.076 nm/s in which grains exhibit zone T growth with fissures between the grains; **(d)** 0.27 Pa / 0.250 nm/s in which the smaller grains are equiaxed; **(e)** 0.67 Pa / 0.250 nm/s in which grains are equiaxed; **(e)** 0.67 Pa / 0.250 nm/s in which grains exhibit zone T growth with fissures between the grains; **(f)** 1.33 Pa / 0.250 n/m/s in which grains exhibit zone T growth with fissures between the grains. White arrows are drawn to aid in identification of some specific grains and fissure features.

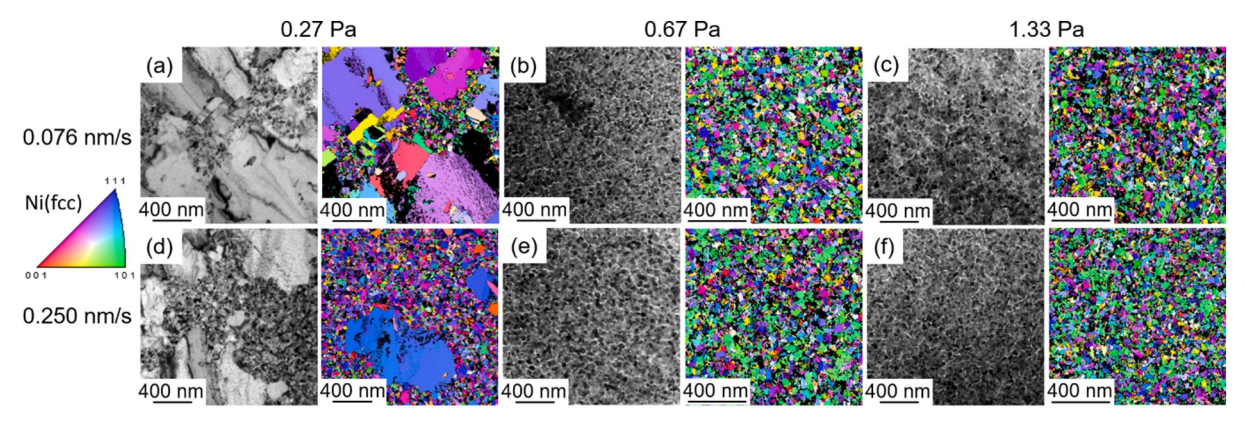


Fig. 3. TEM BF micrographs and orientation maps of the ambient temperature deposited Ni films in plan-view. **(a)** 0.27 Pa / 0.076 nm/s in which a bimodal distribution of grain sizes is observed; **(b)** 0.67 Pa / 0.076 nm/s in which grains are uniform in size and distribution with fissures (bright contrast) between the grains observed; **(c)** 1.33 Pa / 0.076 nm/s in which grains are uniform in size and distribution with fissures between the grains observed; **(d)** 0.27 Pa / 0.250 nm/s in which a bimodal distribution of grain sizes is between the grains observed; **(e)** 0.67 Pa / 0.250 nm/s in which grains are uniform in size and distribution with fissures (bright contrast) between the grains observed; **(f)** 1.33 Pa / 0.250 nm/s in which grains are uniform in size and distribution with fissures (bright contrast) between the grains observed.

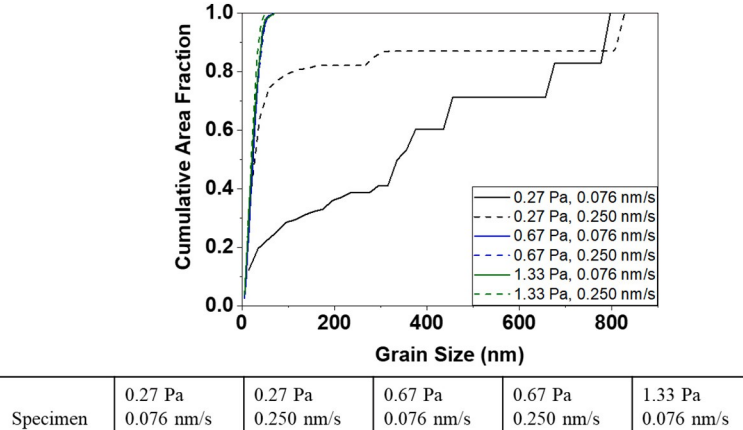
at 0.67 Pa or 1.33 Pa, Fig. 2(b,d,e,f). These surface topologies can be contributed to differences in interfacial energies such as the free surface (during or post deposition) to the columnar grain boundary energy.

Bright field (BF) TEM micrographs in the plan-view orientation confirm the presence of fissures between the grains at the elevated working pressures, Fig. 3(b,c,e,f). A fissure is defined as a linear voided region within the film's microstructure. This fissuring has previously been observed in magnetron sputter deposited Ni thin films between 1.33 and 2.66 Pa and at low sputtering powers. Their formation was attributed to both the high scattering interaction between the Ar and Ni species and the limited mobility of the Ni adatoms [29]. As discussed in the introduction, such grain-to-grain gaps creates a condition for tensile stress generation as the separated regions 'stretch' towards each other to eliminate the free surface and the associated surface energy penalty. Furthermore, a lack of densification also confirms the low adatom mobility that contributes to the tensile stress condition. Between 0.67 Pa and 1.33 Pa, no significant changes in the average grain size or grain size distribution are readily observed by BF TEM imaging. The BF micrographs also reveal a bimodal grain size distribution in films deposited at 0.27 Pa. Qualitatively, a change in the grain texture characteristic is observed across the range of films, changing from a moderate 111 texture at 0.27 Pa to a weak 1/10 texture at 1.33 Pa irrespective of deposition rate. Supplementary pole figures are provided in Appendix A, Fig. A1. While such a change in texture can contribute to stress evolution, the elastic constants in these two orientations are relatively similar [37] and considered to be a less significant influence on the stress evolution as compared to other microstructural features, such as grain size, that will be discussed in Section 3.3 where the stress data is fitted to a kinetic model.

Experimental quantification of the final grain sizes present in these films is displayed via the cumulative area fraction plots, Fig. 4, where the grain sizes were gathered from the PED plan-view orientation mapping. These cumulative area fraction plots reveal drastically different grain size distributions between the films deposited at 0.27 Pa and those deposited at 0.67 Pa or 1.33 Pa. The number of grains counted, which exceeds thousands, for each deposition is tabulated in beneath the cumulative area fraction plot and gives confidence that Fig. 4 is an accurate representation of the grain size distributions for these deposits. Returning to the stress-thickness curves in Fig. 1, the significant upward concavity observed in the 0.27 Pa deposits is likely tied to grain growth in those films during deposition, evident by such different grain sizes in the same deposit.

3.2. Elevated temperature deposits

In conjunction with the influence of the working pressure on the



| Specimen | 0.076 nm/s 20°C | 0.250 nm/s 20°C | 0.076 nm/s 20°C | 0.250 nm/s 20°C | 0.076 nm/s 20°C | 0.250 nm/s 20°C |
|-------------|--------------------|--------------------|--------------------|--------------------|--------------------|--------------------|
| Grain Count | 3648 | 9130 | 4113 | 4207 | 4421 | 4935 |

Fig. 4. Plan-view cumulative area fraction grain size distribution plots of Ni films gathered by PED for all films deposited at ambient temperature and 200 nm thickness. The number of grains counted for each process is provided below the plot.

ambient temperature deposited microstructure and stress-thickness product, the effect of elevating the substrate temperature was also examined. The aim of this was to reduce the fissuring noted at the ambient temperature deposition while still maintaining a sufficiently low homologous temperature to yield an equiaxed, nanocrystalline grain morphology and allow the films to largely remain in the same Thornton zonal regions. The in situ stress thickness measurements are displayed in Fig. 5 for the films deposited at 0.67 Pa and 20 °C (ambient temperature), 100 °C, and 200 °C. Films deposited at 0.076 nm/s display no significant difference between 20 °C and 100 °C in their stress-thickness characteristic and retain a tensile stress state; at 200 °C the film grows in a compressive stress state. This is believed to be a result of the increased mobility of adatoms on the surface that enabled densification of the film.

For the films deposited at the higher rate of 0.250 nm/s, even with a warmer substrate, all deposits exhibited a tensile stress-thickness product. This reveals a growth rate dependence of the stress-thickness product similar to the deposits at ambient temperature shown in Fig. 1. Interestingly, the stress-thickness product indicates that the stress is more tensile at 100 °C than at 20 °C at this deposition rate. This goes against the expected trend that stress becomes more compressive at higher temperatures. This response will be further elaborated upon and understood by the competing balance between multiple temperature-dependent stress mechanisms discussed in detail in the kinetic modeling Section 3.3 below. Further increasing the temperature to 200 °C reverses this behavior to a lower tensile stress-thickness state than that measured at 20 °C.

The dependence of the grain size on the processing conditions (temperature and growth rate) is seen in the plan-view orientation TEM micrographs of Fig. 6. The increased grain size yields a lower grain boundary area fraction, thus increasing the migration distance of the adatom species into the grain boundaries and less collective boundary area to 'stretch' towards. Thus, a complex interaction appears to result from increasing the substrate temperature during deposition. Adatom mobility is enhanced by the increase in substrate temperature and as grain growth occurs, the area fraction of grain boundaries is reduced altering the various mechanisms responsible for tensile stress generation (i.e., mobility and available surface area fraction per volume for 'elastic stretching'). The mosaic of texture colors in the inverse pole figures of Fig. 6 as a function of temperature does not suggest a notable change in texture evolution as previously observed with pressure in Fig. 3. The pole figures for these particular films are found in the Appendix, Fig. A2.

For films deposited at 0.076 nm/s between $20\,^{\circ}$ C and $100\,^{\circ}$ C, only a small amount of grain growth is observed, Fig. 6(a,b), with a distinct

change in the microstructure as noted in terms of the fissure gaps between the grains. Determination of the fissure fractional area by its accumulated area fraction over the entire area imaged observed that the fissuring width corresponded slightly with differences in the fissure area density between these 0.076 nm/s deposits, decreasing from 10.0% of the total area imaged (20 °C) to 8.8% of the total area imaged (100 °C), or a decrease of 12% fissure density between the specimens. An increase in fissuring area fraction would yield a higher contribution of tensile stress. Similarly at 0.250 nm/s, no significant change in fissure area density is observed between 20 °C (15.6%) and 100 °C (15.9%), Fig. 6(d, e), which corresponds to only a 2% increase in fissure density between these deposits. This would imply that the contribution of stress associated with the termination of these fissures is less significant than in those films deposited at 0.076 nm/s. This aids in explaining the increased tensile stress-thickness product observed between 20 $^{\circ}\text{C}$ and 100 $^{\circ}\text{C}$ at 0.250 nm/s while maintaining consistency with those films deposited at 0.076 nm/s.

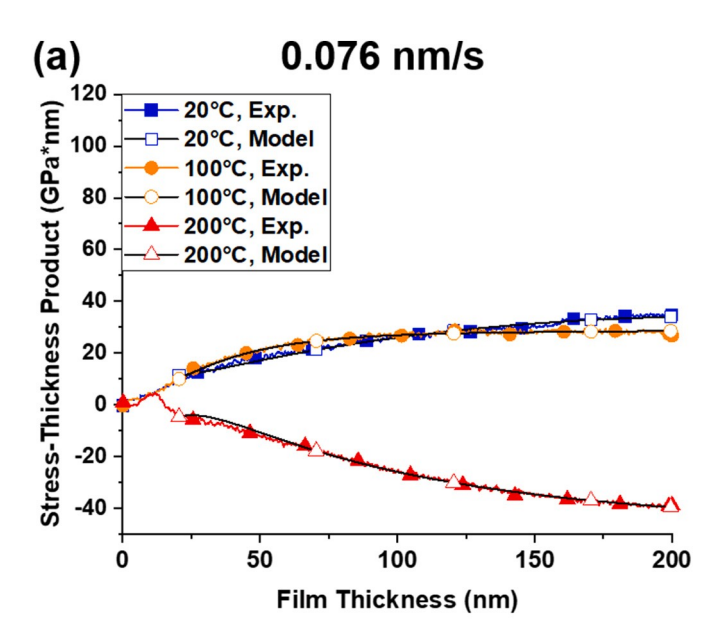
1.33 Pa

At a deposition rate of 0.250 nm/s and 200 °C, grain growth occurs, Fig. 6(f), but appears to be incapable of completely densifying the film. Comparatively, at a lower deposition rate of 0.076 nm/s, the grains grow appreciably and completely densifies the film, Fig. 6(c). The stress-thickness curve corresponding with this low rate, high temperature deposit, Fig. 5(a), displays a compressive growth behavior similar to those films deposited at 0.267 Pa, Fig. 1, wherein significant grain growth and complete densification is reported, Fig. 2(a,d).

Intragranular fissuring is verified in the cross-sectional STEM-HAADF image, Fig. 7, wherein complete densification is only observed at a deposition rate of 0.076 nm/s at 200 °C, Fig. 7(c). Since densification depends on migration of adatom species across the surface of the film before the subsequent layer is formed, this would imply that at the higher deposition rate, wherein the film layers are rapidly increasing in the growth direction, the adatoms have less time to migrate and form a dense film. While increasing the temperature promotes adatom mobility, the extent of densification is clearly limited if the deposition rate increases. Evidently, the grain-growth kinetics clearly vary across this range of temperatures, as revealed by the morphological differences seen in Fig. 7. Initially the grains grow in a columnar manner without the additional substrate heat while subsequent increases in temperature broaden these grains, Fig. 7(c), and/or promote V-shaped growth, Fig. 7 (a,b,d-f). This evolution in zone structure is linked to the general qualitative nature of the Thornton model, where exact zone distinction is not necessarily abrupt or strictly defined. Finally, we note a similar varied surface topology, except for the 0.076 nm/s and 200 $^{\circ}\text{C}$ film where the surface was smooth. This was the only film in this grouping where the

microstructure coalesced. The roughness noted in the other films would be an outcome of varied energy balances between the free surface and grain boundaries.

The cumulative area fraction grain size distributions for the substrate-heated series of films taken in the plan-view via PED are displayed in Fig. 8, with the total count of grains tabulated below it. Reviewing the grain sizes from left to right in this figure, a trend can be gleaned with dependency on both substrate temperature and deposition rate. An increase in temperature yields an increase in grain size in both the low and high-deposition rate conditions. However, the impact of this effect is magnified at the lower deposition rate, wherein the surface adatoms are allowed more time to diffuse and fill intergranular voids before a new surface layer forms, which is supported by the qualitative change in fissuring seen in the STEM cross-sections of Fig. 7.



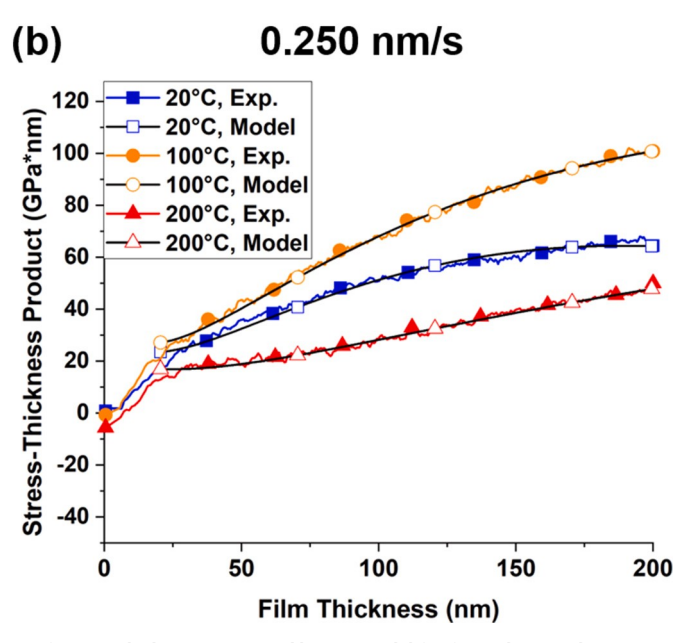


Fig. 5. Stress-thickness curves and kinetic model fits for Ni deposited at 0.67 Pa at substrate temperatures of 20 °C, 100 °C, and 200 °C, and deposition rates of (a) 0.076 nm/s and (b) 0.250 nm/s.

3.3. Comparison with a kinetic model

With the stress-thickness products measured and the films' microstructures quantified, the results are now interpreted and discussed through a kinetic model for thin film stress evolution. As alluded to in the introduction, the kinetic model for sputter deposited films includes energetic conditions during deposition which contribute to the stress generation mechanisms [22,23,32]. It is briefly described here, and the interested reader is directed to the references for further information.

The model describes the stress evolution and corresponding change in wafer curvature with respect to the film thickness, h_f , as the film grows. Defining k as the measured curvature normalized by $M_s h_s^2/6$ enables it to equal to the stress-thickness with the derivative with respect to film thickness given by:

respect to film thickness given by:
$$\frac{\hat{d}k}{dh} = \sigma_c + \sigma \left[\frac{1}{L_{ref}} \right]_{1/2}^{1/2} - \sigma_c e^{\frac{-\beta D}{RL}} + M_f \Delta a \left(\frac{a}{L + a h} \right) \frac{h_f}{L} + a \frac{h}{h} \right] \\
+ A_0 \left[\frac{1}{L} \right]_{1/2}^{1/2} + \left[\frac{1}{L} \right]_{1/2}^{1/2} = \frac{B_0}{L}$$
(2)

The first brace $\{(\sigma_{C_+}.),$ term (I), in eq. (2) corresponds to stress generating processes that occur at the grain boundaries due to non-energetic deposition processes, i.e., kinetic growth. Here, R is the film growth rate and L refers to the grain size at the surface of the film while $M_P \Delta a$ is the product of the biaxial modulus of the film and the width of the grain boundary. σ_C is the compressive stress due to elevation of the chemical potential on the surface during deposition, $\sigma_{T,0}$ describes the tensile stress due to island coalescence at the grain size of L_{ref} . For other grain sizes, the tensile stress is adjusted by $(L_{ref}/L)^{1/2}$. In order to include the temperature dependence, the term βD is parameterized as (1/kT) $(\beta D)_0 \exp(-E_A/kT)$, where k is Boltzmann's constant, T is the substrate temperature, E_A is the activation energy, and βD is a kinetic parameter describing the growth rate dependence for the transition between tensile and compressive stress.

The second brace $\{M_{fl}a\ldots\}$, term (II), includes the potential effect of grain growth within the film during deposition. The grain size at the surface and the film/substrate interface are assumed to change linearly with the film thickness at potentially different rates. The grain size at the surface is given by $L_0+\alpha_2h_f$ and the grain size at the film substrate interface is $L_0+\alpha_lh_f$. The grain size at other depths in the film is assumed to change linearly between these values from the bottom to the top. The grain growth parameters $(L_0, \alpha_l, and \alpha_2)$ are determined by fitting the data to the model. Controlling the relationship between α_1 and α_2 enables the different types of microstructural evolution in the Thornton model [20] to be modeled, i.e., $\alpha_l=0$ for zone T and $\alpha_l=\alpha_2$ for zones 1 and 2.

The next two braces, $\{A_o(l/L)\}\$ and $\{(I-(l/L))...\}$, terms (III) and (IV) respectively, are intended to model energetic particle effects during sputter deposition. Term (III) represents stress-inducing densification near the grain boundary and term (IV) models the stress induced by defect generation and trapping in the film. τ_s is the characteristic time it takes for a defect created at depth l to diffuse with a rate D_i to the surface. While the experimental stress measurement is a collective response, term (IV) assists in deconvoluting the defect stress contributions between the grain interior and grain boundaries from the aforementioned mechanisms discussed in the introduction. For example, the stress from 'atomic peening' that is created from the momentum transfer of arriving energetic particles can create defects in either the bulk of the film and/or at the grain boundaries which would be captured by this term. In order to reduce the number of free parameters, A_o , the parameter describing densification stress, B_o , the defect trapping stress contribution, and l, the implantation depth of energetic particles, are assumed to depend linearly on the pressure above a critical value P_0 . Therefore, for each pressure we use $A_o = A*(1-P/P_o)$ so that there is only one parameter, A*, for

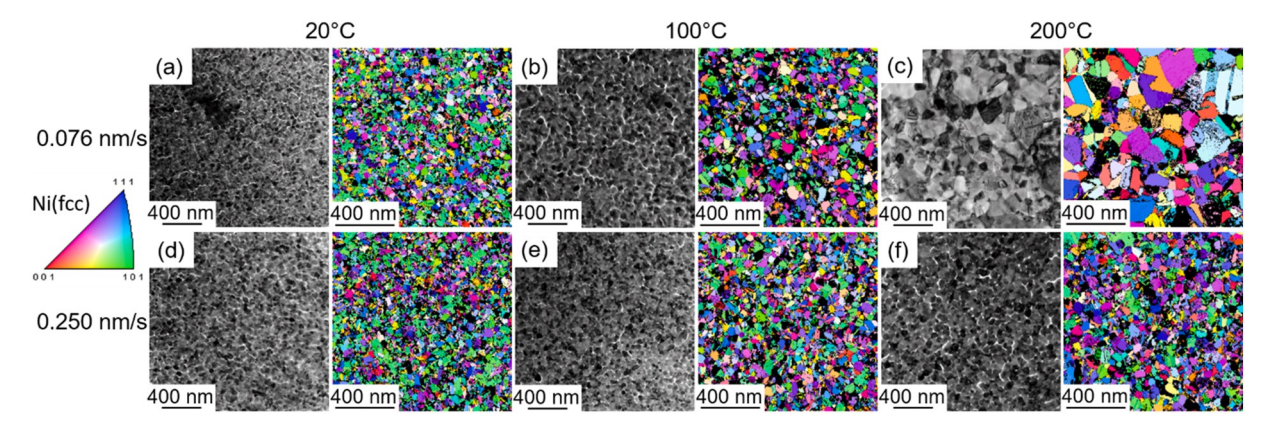


Fig. 6. TEM bright field micrographs and orientation maps of Ni films in plan-view deposited at 0.67 Pa and **(a)** 20 °C / 0.076 nm/s in which grains are uniform in size and distribution with fissures observed (bright contrast); **(b)** 100 °C / 0.076 nm/s in which grains are uniform in size and distribution with finer fissures (bright contrast) between the grains observed; **(c)** 200 °C/0.076 nm/s in which no fissures are observed and average grain size is significantly increased; **(d)** 20 °C/0.250 nm/s nm/s in which grains are uniform in size and distribution with fissures (bright contrast) between the grains observed; **(e)** 100 °C / 0.250 nm/s in which grains are uniform in size and distribution with finer fissures (bright contrast) between the grains observed; **(f)** 200 °C / 0.250 nm/s in which grains are slightly large, uniform in size and distribution, with fissures between the grains observed.(10%) (8.8%).

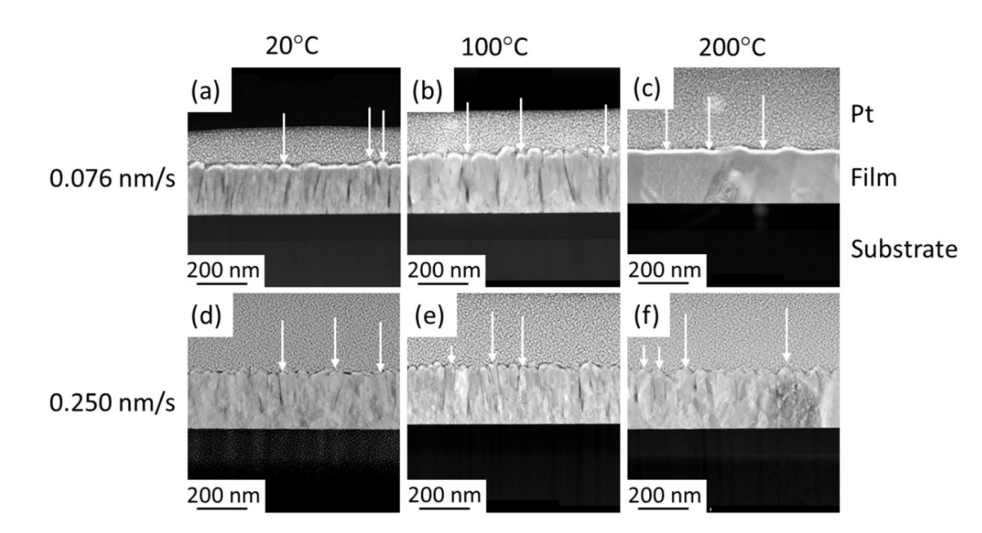


Fig. 7. STEM micrographs of Ni films in cross-section deposited at 0.67 Pa and **(a)** 20 °C/0.076 nm/s in which grains exhibit zone T growth with fissures observed; **(b)** 100 °C/0.076 nm/s in which grains exhibit zone T growth with fissures between the grains is observed; **(c)** 200 °C / 0.076 nm/s in which grains exhibit zone T growth; **(d)** 20 °C / 0.250 nm/s in which grains exhibit zone T growth with fissures between the grains; **(e)** 100 °C / 0.250 nm/s in which grains exhibit zone T growth with finer fissures between the grains; **(f)** 200 °C / 0.250 nm/s in which grains exhibit zone T growth with finer fissures between the grains; **(f)** 200 °C / 0.250 nm/s in which grains exhibit zone T growth morphologies with fissures between the grains. White arrows are drawn to aid in identification of some specific grains and their features

multiple pressures (and similarly for B^* and I^*). This dramatically reduces the number of fitting parameters that need to be considered.

The model in Eq. (2) is integrated over the thickness to obtain the curvature vs. thickness for comparison to the experimental measurements. A non-linear least squares fitting procedure produces a set of kinetic parameters that minimize the residual between the calculation and the data. The range from 20 to 200 nm is evaluated as we consider only the region where the film is continuous (i.e., post-coalescence).

It is important to note that each data set was not fit separately with a different set of parameters. Since some parameters should be the same for all the data, multiple sets of data were fitted at the same time and some parameters were set to be common to all the data sets while others were allowed to vary independently for each set. To that end, the fitting parameters $\sigma_{T,25mm}$, $(\beta D)_0$, E_A , $M_1 \Delta a$, P_0 , A^* , B^* and I^* were made to be common for all the data sets with their results tabulated in Table 1 with the value of the tensile stress given in this table being for a reference grain size of 25 nm, corresponding to the post-coalescence regime. The remaining parameters $(\sigma_C, D_i, L_0, \alpha_I, \alpha_2)$ were allowed to vary for each of

the measurements made at the different growth rates, pressures, and temperatures, as described earlier. These are reported in Table 2. Fig. 9 shows the individual contributions of the four terms in Eq. (2) so that one can see their relative contributions to the total stress fit shown for either Fig. 1 or Fig. 5.

For comparison, the second row of Table 1 tabulates the parameters for Ni stress deposited under non-energetic conditions [38]. Comparing the same parameters between energetic and non-energetic conditions, one can note that they are similar which suggests that the non-energetic growth processes leading to stress are similar for either evaporation or sputter deposition.

The dependence of σ_C on T and R for the sputtered Ni can be seen in Table 2. The dependence of σ_C on the growth parameters is difficult to determine precisely from the small range studied. However, the parameters fall within the same range as those obtained for evaporated Ni, suggesting that the degree of supersaturation leading to compressive stress is similar for both cases.

From Table 2, we also note the growth zone factor values of α_1 and

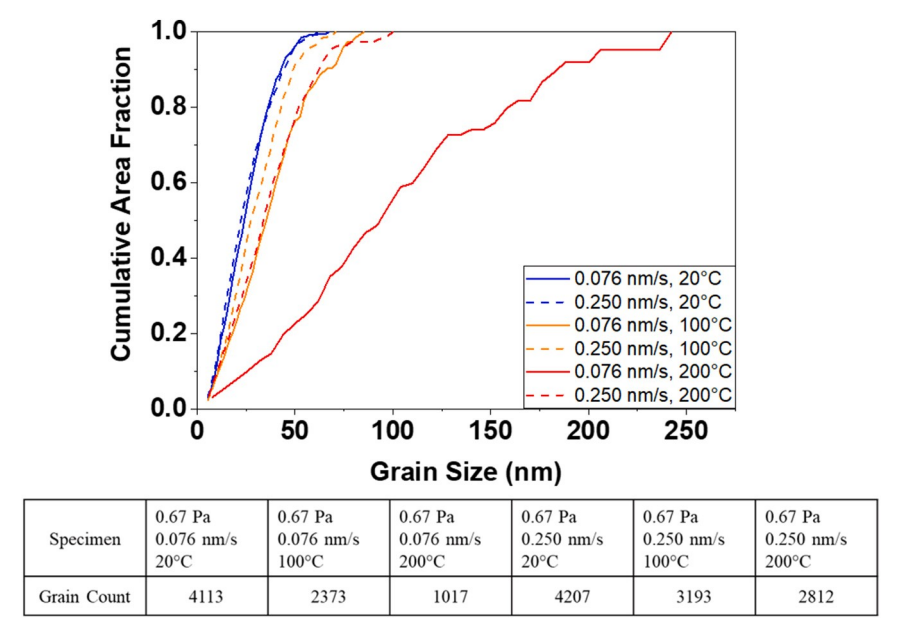


Fig. 8. Plan-view cumulative area fraction grain size distribution plots of 200 nm thick Ni films deposited at 0.67 Pa gathered by PED. An increase in average grain size is observed as the substrate is heated, with its influence more prevalent at lower deposition rates. The number of grains counted for each process is provided below the plot.

Table 1
Common fitting parameters determined from fitting the kinetic model to sputter deposited Ni from this work and those from an e-beam evaporated Ni film calculated at a reference grain size of 25 nm [32].

| Common parameters | σ _{T,25nm} (GPa) | (βD) ₀ (nm ² /s) | E _A (eV) | M _f ∆a (GPa*nm) | P ₀ (Pa) | A* (GPa) | B* (GPa) | l* (nm) |
|-------------------|---------------------------|---|------------------------|-------------------------------|------------------------|----------|----------|------------|
| Sputtered Ni | 1.01 | 1.60 | 0.101 | 31.0 | 2.28 | -2.60 | -6.77 | 2.11 |
| Evaporated Ni | 1.57 | 2.62 | 0.117 | 26.1 | N/A | N/A | N/A | N/A |

Table 2
Parameters permitted to vary across specimens in fitting a kinetic model to experimental data presented. Note that for the 0.25 nm/s / 0.27 Pa film, the standard deviation is larger than the average; this is a result of the large bimodal grain size distribution in this sample and clearly for the smaller grain sizes, any negative value is unphysical. Nevertheless, the use of an experimental average grain size provides for a direct comparison to the singular grain size outputted from the fit to the kinetic model.

| Deposition condition | σ _c (GPa) | $D_i (nm^2/s)$ | α_1 | α_2 | Calculated surface grain size | Measured Avg. grain size | |
|---------------------------------|----------------------|----------------|------------|------------|--------------------------------|--------------------------------|--|
| | | | | | at $h_f = 200 \text{ nm (nm)}$ | at $h_f = 200 \text{ nm (nm)}$ | |
| 0.250 nm/s 0.67 Pa, RT | -0.195 | 1.73 | 0.0409 | 0.1265 | 28 | 25 ± 13 | |
| 0.250 nm/s 0.67 Pa, 100 °C | -0.923 | 2.30 | 0.0689 | 0.1610 | 34 | 30 ± 15 | |
| 0.250 nm/s 0.67 Pa, 200 °C | -2.20 | 4.65 | 0.0918 | 0.1957 | 40 | 37 ± 20 | |
| 0.076 nm/s 0.67 Pa, RT | -1.67 | 0.876 | 0.0777 | 0.1320 | 28 | 26 ± 13 | |
| 0.076 nm/s 0.67 Pa, 100 °C | -1.33 | 1.64 | 0.0987 | 0.1739 | 36 | 38 ± 20 | |
| 0.076 nm/s 0.67 Pa, 200 °C | -1.29 | 3.00 | 0.0998 | 0.4678 | 89 | 104 ± 61 | |
| 0.250 nm/s 0.27 Pa, | -1.62 | 6.91 | 0.0054 | 0.0696 | 19 | 154 ± 273 | |
| RT 0.250 nm/s 1.33 Pa, | -3.81 | 0.879 | 0.0589 | 0.1150 | 24 | 22 ± 11 | |
| RT 0.076 nm/s 0.27 Pa, | -0.0094 | 9.94 | 0.0060 | 0.0425 | 10 | 370 ± 290 | |
| RT 0.076 nm/s 1.33 Pa, RT | -1.77 | 0.343 | 0.0756 | 0.1228 | 26 | 24 ± 13 | |

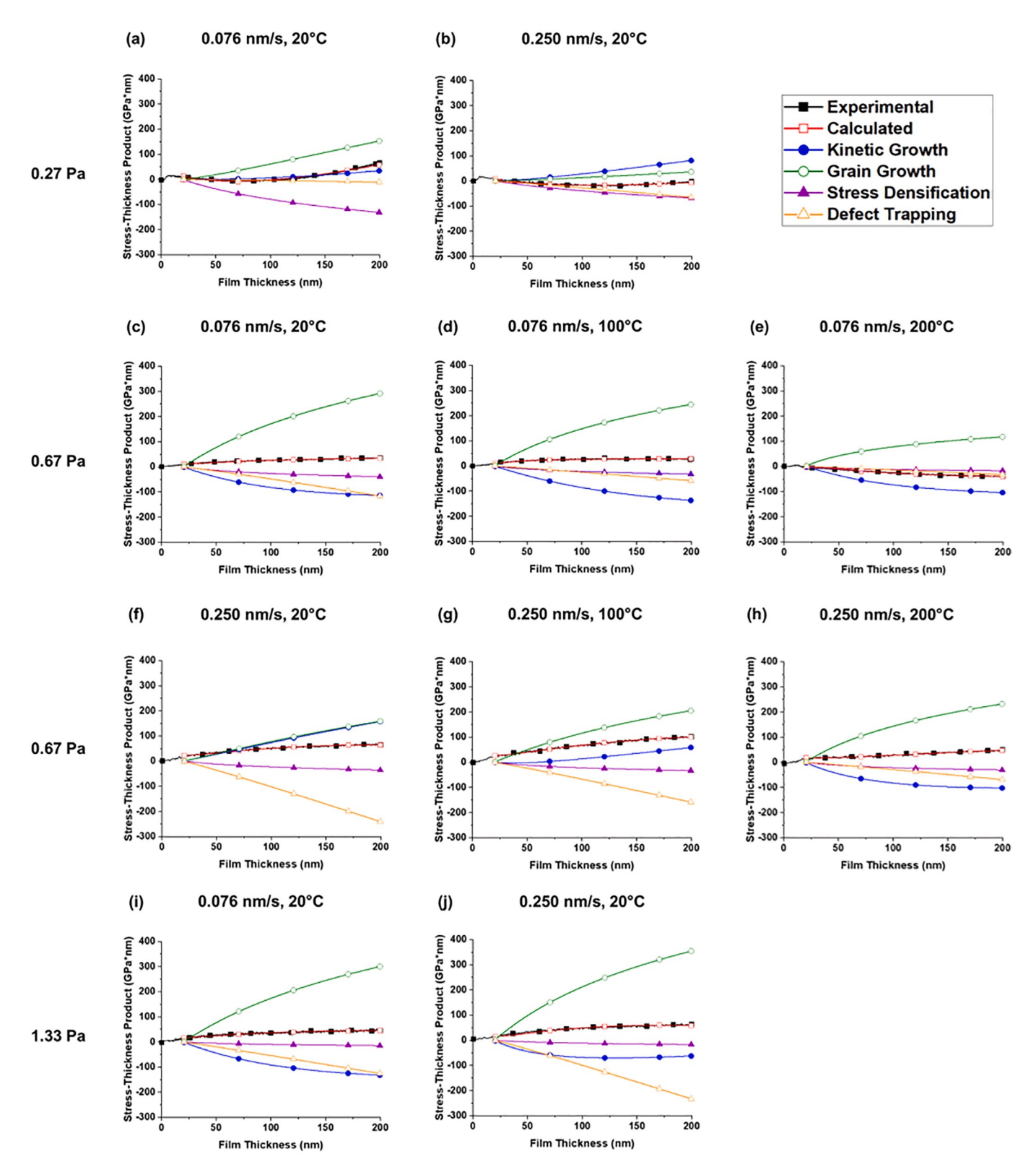


Fig. 9. Stress-thickness plots detailing the contributions to the calculated stress-thickness product from I (kinetic growth/blue curve with filled circle), II (grain growth/green curve with open circle), III (stress densification/purple curve with filled triangle), and IV (defect trapping/orange curve with open triangle) mechanisms.

 $\alpha_2.$ Since $\alpha_1\approx 0,$ this would favor a Zone T growth behavior [17]. Based on the processing conditions used, T_m $\underline{0}.17$ at 0.67 Pa or 1.33 Pa, the films are predicted to fall on the border of Zone 1 and Zone T, which was consistent with the microstructural features captured in the cross-sectional STEM images of Fig. 2. The films are not fully densified at either 0.67 Pa or 1.33 Pa, evident by the darker lines in the STEM images (i.e., no signal detected). These intergranular fissures are expected to occur in the Zone 1 growth regime. Nevertheless, the grains also maintain the V-shaped blossoming associated with Zone T, which matches the kinetic model prediction. Of these films, the 0.27 Pa deposition was the exception in that it did not reveal a clear columnar or V-shape structure in cross-section. This will be addressed further below with respect to its bimodal grain size distribution.

The value of D_i produced by the fitting with values tabulated in Table 2 is different for each temperature and is explained by an Arrhenius temperature-dependence with an activation energy of $0.073 \pm$ 0.012 eV. The value of D_i also depends inversely on the grain size, which suggests that grain boundary diffusion may play a greater role in defect transport when the grain size becomes ever smaller. Furthermore, the growth stress is generally expected to become less tensile at higher temperatures because of the higher mobility of adatoms on the surface. However, as noted above, the film deposited at 100 °C is significantly more tensile than at ambient temperature for the 0.250 nm/s growth rate, Fig. 5. The fitting parameters, Table 2, suggest that this can be partially attributed to the temperature dependence of D_{ij} which corresponds to higher defect diffusivity at higher temperatures. An increase in the diffusivity promotes the escape of ion-induced defects which reduces the compressive stress. In addition, faster grain growth kinetics at higher temperature can facilitate more tensile stress generation. At 200 °C, this trend reverses and the stress becomes more compressive. According to the fitting parameters, Table 2, this is because the stress associated with non-energetic growth processes becomes more compressive with increasing temperature.

The dependence of the stress evolution on the growth conditions and microstructural evolution is clearly complex, so use of the kinetic model to aid interpretation is helpful in explaining observed trends. The individual contributions of the terms in the model to the fitting are shown for each data set in Fig. 9. The total model fit is plotted as the unfilled red squares for comparison to the filled black squares for measured stress-thickness. The other curves correspond to the different terms in the model in Eq. (2). The contribution of the non-energetic growth term (I) is shown in blue circles (labelled kinetic growth). The contribution of the grain growth term (II) is shown in green circles (labelled grain growth). The two contributions of the energetic growth (III and IV) are shown in purple triangles (labelled stress densification) and orange triangles (labelled defect trapping).

Using Fig. 9, we can ascertain which contributions (non-energetic vs. energetic) contribute more or less to the overall stress evolution. In general, lower pressure is associated with higher energies for the incoming adatoms and leads to more compressive stress. This is seen in the more compressive stress for films deposited at the lowest pressure (0.27 Pa) for both growth rates, where the stress densification (purple curve) dominates, Fig. 9(a,b). With an increasing deposition rate at these pressures, we do note the additional contribution of the defect trapping (orange curve) becomes more compressive while the grain growth (green) and kinetic growth (blue) are both tensile but invert in their absolute value contributions to the overall stress evolution.

In general, the stress becomes less dependent on the pressure at higher pressures. This is primarily attributed to the fact that the energy of the particles decreases as the pressure increases so that their energetic contributions to the stress become less significant. An exception is seen for the growth rate of 0.250 nm/s at ambient temperature, where the stress is actually slightly more tensile for 0.67 Pa than it is for 1.33 Pa. The fitting parameters suggest this is because of an increase in the grain growth-induced tensile stress that compensates for the change in the sputter-induced compressive stress with pressure. This illustrates

applicability of the model to elucidate the underlying mechanisms' contributions to how the stress evolves.

Finally, the grain size at the surface is another parameter that can be compared between the experimentally measured values and the results obtained from the fitting. The values obtained from the fitting and the measurement are shown in Table 2 columns six and seven respectively. The results are very similar with the notable exceptions of the ambient temperature depositions at 0.27 Pa, which is further discussed below.

The measured average surface grain size is plotted relative to the predicted size from the fitting at 200 nm in Fig. 10. Leaving out the anomalous results at 0.27 Pa, we see a linear correlation of >99% between the two sets of parameters. This provides further confidence in the model's ability to extract stress contribution values (as discussed above for the non-energetic terms) and microstructural values (grain size) that contributes to the stress.

The large difference between the measured grain size and the fitting at 0.27 Pa can be explained by looking more closely at the measured grain size distribution in these films. Unlike the other films, which have a relatively uniform grain size, the grain size distribution in these two films is bimodal with many large grains. In comparison, the model assumes a singular grain size. Therefore, reporting grain size results by fitting to the model may not be as reliable when grain sizes distributions diverge significantly. Interestingly, the model is able to do a reasonable job of fitting the stress-thickness evolution for these two films, Fig. 1, even though the grain size parameter may not be correct. This supports that representative characterization of grain sizes should be done in conjunction with any model fitting. The fact that the fitting parameter is much smaller than the average measured grain size may suggest that the small grains dominate in the development of the stress. However, the grain size distribution for these two outliers may also provide some contribution that is not yet captured in the current model.

Though the fittings to the model add insight to the underlying mechanisms responsible for the stress evolution, we emphasize that different sets of parameters than those shown here could, in principle, yield reasonable fits too. Furthermore, the lack of capturing texture evolution effects as well as surface topology evolution (rough vs. smooth surfaces) are not yet included factors within the kinetic model but offer potential, future modifications. Therefore, the model should be used to suggest trends in the stress evolution and guide the extent of each mechanism used in the model in interpreting the data even if the absolute value may not be exact. The use of other means of deposition, such as a comparison with non-energetic contributions using non-energetic deposition measurements, as well as correlation of predicted grain sizes to measured grain sizes, can provide confidence that the fits are reasonable such that energetic contributions, and their associated values, are accurate representations in their contributions.

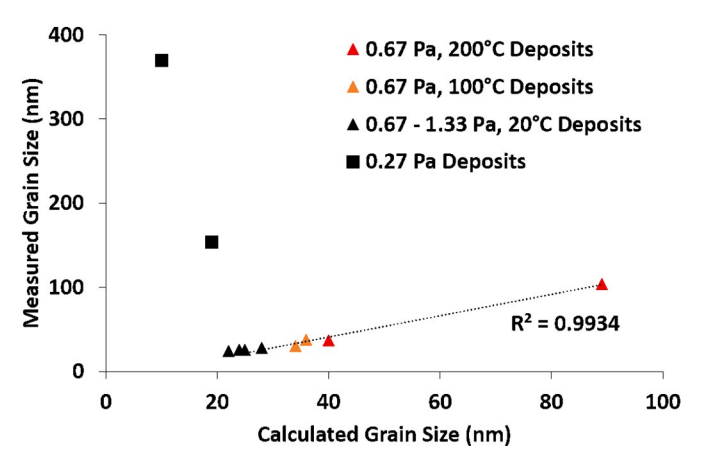


Fig. 10. Correlation of the measured and calculated grain sizes. Note that the 0.27 Pa deposits are outliers and are excluded in plotting the linear correlation.

4. Conclusions

A series of Ni thin films have been sputter deposited onto a thermally grown amorphous silica surface present on Si substrates across an array of deposition rates, working pressures, and substrate temperatures. Films deposited at the ambient temperature at 0.27 Pa had a bimodal grain size distribution across a wide range of 20–800 nm. In contrast, films deposited at 0.67 Pa and 1.33 Pa maintained a narrow nanocrystalline grain size structure but with incomplete densification between the grain boundaries evident by fissures. These microstructural differences contributed to the stress-thickness product evolution, with trends demonstrating an increase in tensile stress responses with pressure.

Films deposited at elevated temperatures, $100\,^{\circ}$ C and $200\,^{\circ}$ C, at $0.67\,^{\circ}$ Pa, revealed an increase in film densification by enhancing the adatom mobility at the expense of grain growth. These films lie on the border between Zone 1 and Zone T in the Thornton model which was observed by the cross-sectional electron microscopy imaging.

Using both the microstructural quantification and the stress measurements, a kinetic model for stress-thickness evolution was employed to assist with relating the stress-thickness product with the microstructural development. Fitting the model to the experimental data was able to reproduce the dependence of the stress evolution on temperature and growth rate. The parameters corresponding to non-energetic stress-generating processes in the model are similar to those reported from analysis of non-energetic using evaporation. This suggests that the non-energetic processes are similar for both sputtering and evaporation. The model also provided a predicted grain size, which matched well for all deposition conditions to the experimental measurement of the final grain size except for the ambient temperature, 0.27 Pa deposition. Here, the experimental grain sizes distribution was bimodal. The current model's ability to use only a single value for grain size contributes to the deviation of the fit to the experimental value; nevertheless, it was still

sufficient to still capture the stress evolution trend. This paper provides furthers insights into Ni's stress evolution under sputter deposition as well as the use of a kinetic model to understand the various contributions to such stress.

Declaration of competing interest

The authors declare that they have no known competing financial interests or personal relationships that could have appeared to influence the work reported in this paper.

Acknowledgements

TRK, GT, and GBT gratefully acknowledge the support of the Army Research Office grant W911NF-17-1-0528, Dr. Michael Bakas, program manager. ZR and EC acknowledge NSF-DMR-1602491 and DMR-2006422.

CRediT authorship contribution statement

Thomas Koenig – oversaw the initial draft and performed all the experimental depositions, measurements and characterization.

Zhaoxia Rao $-\,\mathrm{performed}$ the kinetic modeling fitting to the stress evolution data.

Eric Chason – assisted in writing and editing the paper, with particular emphasis to the kinetic model. Secured funding from NSF to perform the research.

Garritt Tucker – provided technical input on the manuscript and film growth selection. Secured funding from ARO to perform the research.

Gregory B. Thompson – oversaw the overall program objectives and provided technical input on the deposition and characterization methodologies. Secured funding from ARO to perform the research.

Appendix A. Pole figures from planview PED data and SIMTRA modeling constraint data

Table A1Inputs and constraints applied to SIMTRA [39] for calculating the average arrival energy of Ni species on a planar substrate.

| SIMTRA parameter | Input value |
|---|----------------------------|
| Chamber length (m) | 0.33 |
| Chamber radius (m) | 0.33 |
| Chamber temperature (K) | 300 |
| Number of particles | 876,000 |
| Target element | Ni |
| Target shape | Planar |
| Target thickness (m) | 0.00635 |
| Target radius (m) | 0.0254 |
| Throw distance (m) | 0.16 |
| Substrate diameter (m) | 0.0254 |
| Racetrack type | racetrackGent |
| Angular distribution Interaction potential | C_1 = 1; else 0 Moliere |

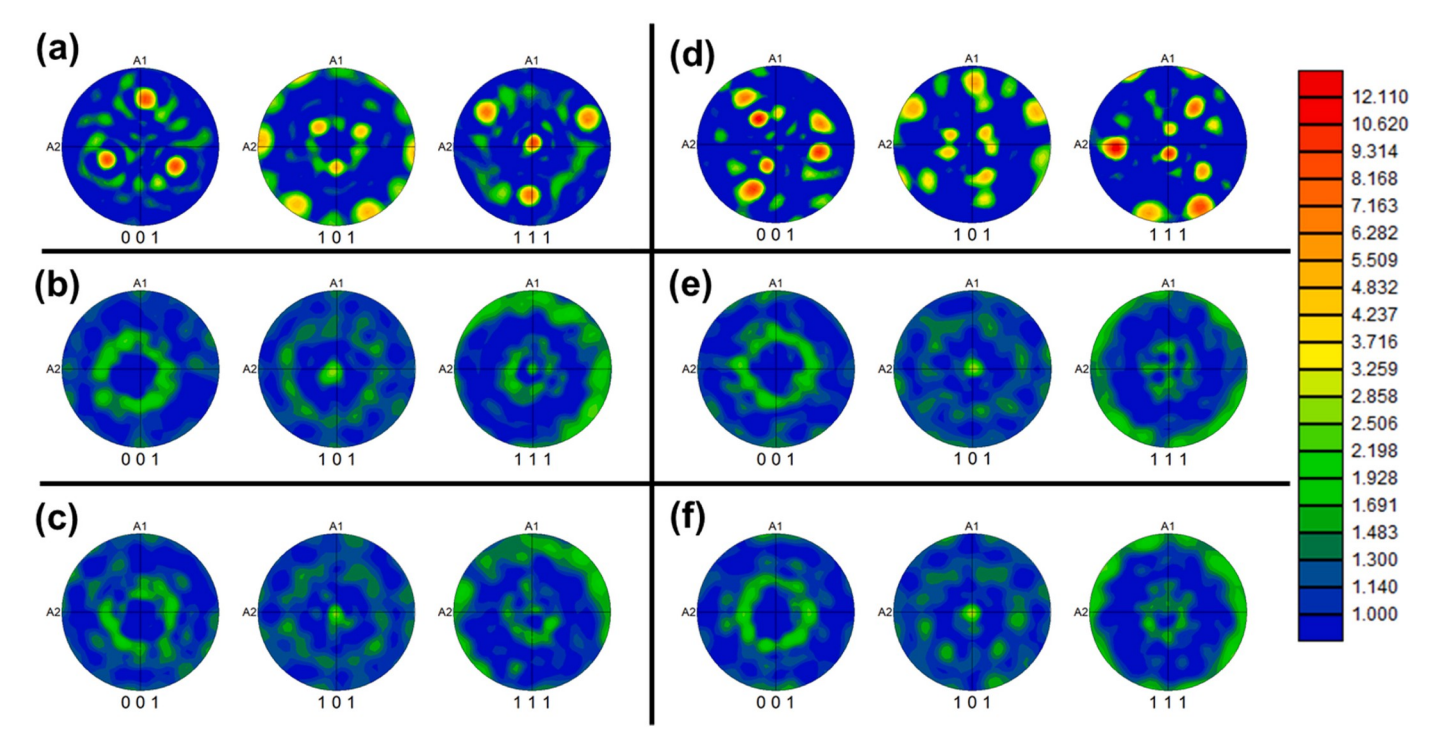


Fig. A1. PFs produced from PED data gathered in plan-view of 200 nm thick Ni films deposited at (a)—(c) 0.076 nm/s and (d)—(f) 0.250 nm/s. (a,d) 0.27 Pa which displays a strong <111> texture, (b,e) 0.67 Pa which displays a weak <110> texture, and (c,f) 1.33 Pa which displays a weak <110> texture.

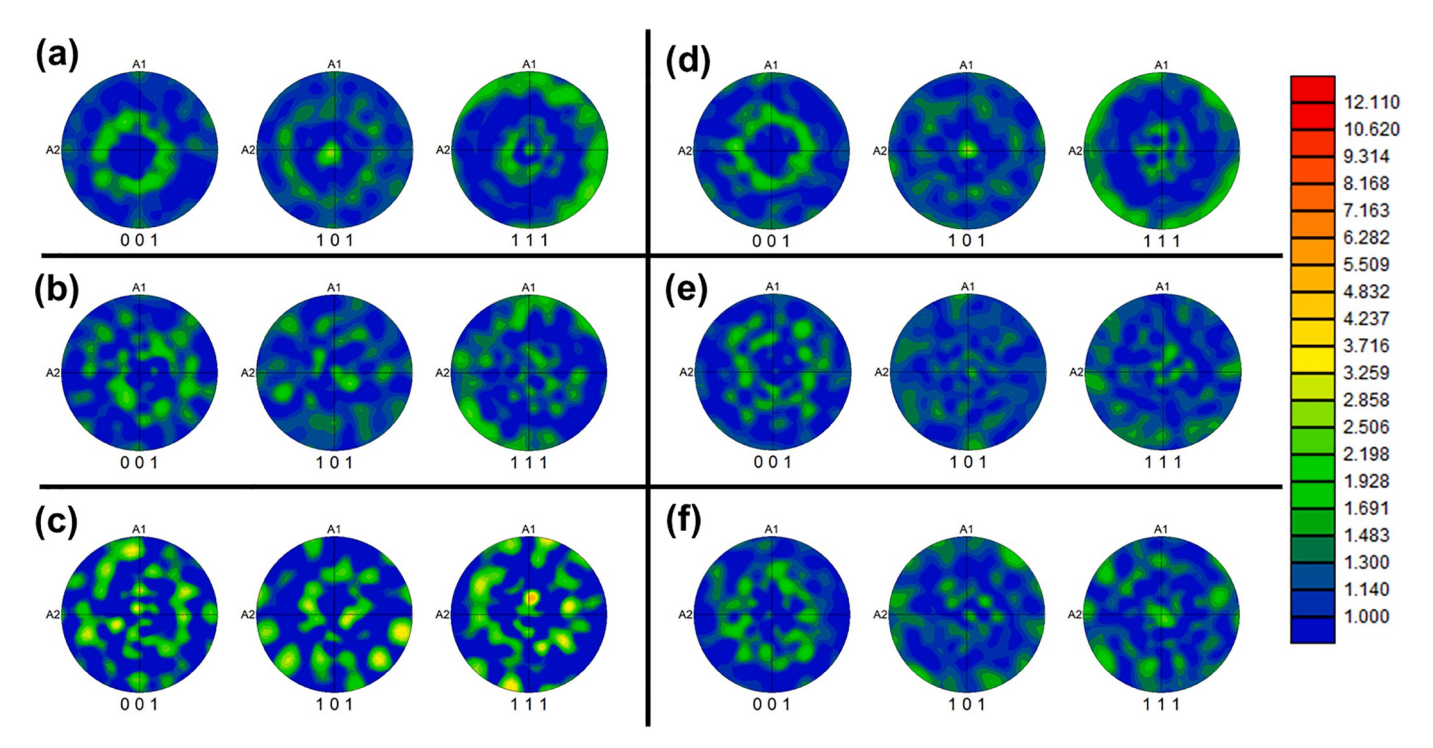


Fig. A2. PFs produced from PED data gathered in plan-view of 200 nm thick Ni films deposited at 0.67 Pa and (a)–(c) 0.076 nm/s and (d)–(f) 0.250 nm/s. (a,d) Room temperature deposits which displays a weak <110> texture; (b,e) 100 °C which displays no significant preference in texture; and (c,f) 200 °C which displays a weak <111> texture.

References

- [1] A.A. Navid, E. Chason, A.M. Hodge, Evaluation of stress during and after sputter deposition of Cu and Ta films, Surf. Coat. Technol. 205 (2010) 2355–2361, https://doi.org/10.1016/j.surfcoat.2010.09.020.
- [2] H.Z. Yu, C.V. Thompson, Grain growth and complex stress evolution during Volmer–Weber growth of polycrystalline thin films, Acta Mater. 67 (2014) 189–198, https://doi.org/10.1016/j.actamat.2013.12.031.
- [3] S.J. Hearne, J.A. Floro, Mechanisms inducing compressive stress during electrodeposition of Ni, J. Appl. Phys. 97 (2005), 014901, https://doi.org/ 10.1063/1.1819972.
- [4] G.C.A.M. Janssen, Stress and strain in polycrystalline thin films, Thin Solid Films 515 (2007) 6654–6664, https://doi.org/10.1016/j.tsf.2007.03.007.
- [5] R. Koch, Stress in evaporated and sputtered thin films a comparison, surf, Coat. Technol. 204 (2010) 1973–1982, https://doi.org/10.1016/j.surfcoat.2009.09.047.
- [6] M.-W. Moon, J.-W. Chung, K.-R. Lee, K.H. Oh, R. Wang, A.G. Evans, An experimental study of the influence of imperfections on the buckling of compressed thin films, Acta Mater. 50 (2002) 1219–1227, https://doi.org/10.1016/S1359-6454(01)00423-2.
- [7] V.B. Shenoy, A.F. Schwartzman, L.B. Freund, Crack patterns in brittle thin films, (n. d.) 17.
- [8] G. Gore, On the properties of electro-deposited antimony, Philos, Trans. R. Soc. Lond. 148 (1858) 185–197, https://doi.org/10.1098/rstl.1858.0010.
- [9] R. Koch, D. Hu, A.K. Das, Compressive stress in polycrystalline Volmer-Weber films, Phys. Rev. Lett. 94 (2005), https://doi.org/10.1103/ PhysRevLett.94.146101.
- [10] F. Spaepen, Interfaces and stresses in thin films, Acta Mater. (2000) 31–42, https://doi.org/10.1016/S1359-6454(99)00286-4.
- [11] E. Chason, B.W. Sheldon, L.B. Freund, J.A. Floro, S.J. Hearne, Origin of compressive residual stress in polycrystalline thin films, Phys. Rev. Lett. 88 (2002), https://doi.org/10.1103/PhysRevLett.88.156103.
- [12] R.C. Cammarata, T.M. Trimble, D.J. Srolovitz, Surface stress model for intrinsic stresses in thin films, J. Mater. Res. 15 (2000) 2468–2474, https://doi.org/ 10.1557/JMR.2000.0354.
- [13] C. Friesen, S.C. Seel, C.V. Thompson, Reversible stress changes at all stages of Volmer–Weber film growth, J. Appl. Phys. 95 (2004) 1011–1020, https://doi.org/ 10.1063/1.1637728.
- [14] A. Schell-Sorokin, R. Tromp, Mechanical stresses in (sub)monolayer epitaxial films, Phys. Rev. Lett. 64 (1990) 1039–1042, https://doi.org/10.1103/ PhysRevLett.64.1039.
- [15] S.G. Mayr, R.S. Averback, Effect of ion bombardment on stress in thin metal films, Phys. Rev. B 68 (2003), https://doi.org/10.1103/PhysRevB.68.214105.
- [16] S.C. Seel, C.V. Thompson, Piezoresistive microcantilevers for in situ stress measurements during thin film deposition, Rev. Sci. Instrum. 76 (2005), 075103, https://doi.org/10.1063/1.1947067.
- [17] E. Chason, P.R. Guduru, Tutorial, Understanding residual stress in polycrystalline thin films through real-time measurements and physical models, J. Appl. Phys. 119 (2016), 191101, https://doi.org/10.1063/1.4949263.
- [18] A.M. Engwall, Z. Rao, E. Chason, Origins of residual stress in thin films: interaction between microstructure and growth kinetics, Mater. Des. 110 (2016) 616–623, https://doi.org/10.1016/j.matdes.2016.07.089.
- [19] W.D. Nix, B.M. Clemens, Crystallite coalescence: a mechanism for intrinsic tensile stresses in thin films, J. Mater. Res. 14 (1999) 3467–3473, https://doi.org/ 10.1557/JMR.1999.0468.
- [20] J.A. Thornton, D.W. Hoffmam, Stress-related effects in thin films, Thin Solid Films 171 (1989) 5–31, https://doi.org/10.1016/0040-6090(89)90030-8.

- [21] F.M. D'Heurle, J.M.E. Harper, Note on the origin of intrinsic stresses in films deposited via evaporation and sputtering, Thin Solid Films 171 (1989) 81–92, https://doi.org/10.1016/0040-6090(89)90035-7.
- [22] T.M. Kaub, Z. Rao, E. Chason, G.B. Thompson, The influence of deposition parameters on the stress evolution of sputter deposited copper, Surf. Coat. Technol. 357 (2019) 939–946.
- [23] E. Chason, M. Karlson, J.J. Colin, D. Magnfält, K. Sarakinos, G. Abadias, A kinetic model for stress generation in thin films grown from energetic vapor fluxes, J. Appl. Phys. 119 (2016), 145307, https://doi.org/10.1063/1.4946039.
- [24] S. Itapu, Microstructuring of Nickel Thin Films and Property Modification of Nickel Oxide Films by Pulsed Laser Irradiation, The University of Toledo, 2017.
- [25] V.N. Sekhar, V. Srinivasarao, R. Jayaganthan, K. Mohankumar, A.A.O. Tay, A study on the mechanical behavior of the sputtered nickel thin films for UBM applications, in: Proc. 6th Electron. Packag. Technol. Conf. EPTC 2004 IEEE Cat No04EX971, IEEE, Singapore, 2004, pp. 610–614, https://doi.org/10.1109/ EPTC.2004.1396680.
- [26] J. Kim, W. Jang, J. Park, H. Jeon, H. Kim, J. Yuh, H. Jeon, Characteristics of a nickel thin film and formation of nickel silicide by using remote plasma atomic layer deposition with Ni(iPr-DAD)2, J. Korean Phys. Soc. 66 (2015) 821–827, https://doi.org/10.3938/jkps.66.821.
- [27] C.V. Thompson, R. Carel, Stress and grain growth in thin films, J. Mech. Phys. Solids. 44 (1996) 657–673, https://doi.org/10.1016/0022-5096(96)00022-1.
- [28] I. Petrov, P.B. Barna, L. Hultman, J.E. Greene, Microstructural evolution during film growth, J. Vac. Sci. Technol. A 21 (2003) 13.
- [29] B. Geetha Priyadarshini, S. Aich, M. Chakraborty, Structural and morphological investigations on DC-magnetron-sputtered nickel films deposited on Si (100), J. Mater. Sci. 46 (2011) 2860–2873, https://doi.org/10.1007/s10853-010-5160-6.
- [30] A. Sharma, S. Mohan, S. Suwas, The influence of deposition temperature on the structure, microstructure, morphology and magnetic properties of sputter deposited nickel thin films, Thin Solid Films 619 (2016) 91–101, https://doi.org/ 10.1016/j.tsf.2016.10.024.
- [31] J.A. Thornton, D.W. Hoffman, Internal stresses in titanium, nickel, molybdenum, and tantalum films deposited by cylindrical magnetron sputtering, J. Vac. Sci. Technol. 14 (1977) 164–168, https://doi.org/10.1116/1.569113.
- [32] E. Chason, A.M. Engwall, Z. Rao, T. Nishimura, Kinetic model for thin film stress including the effect of grain growth, J. Appl. Phys. 123 (2018), 185305, https://doi.org/10.1063/1.5030740.
- [33] L.B. Freund, S. Suresh, Thin Film Materials Stress, Defect Formation and Surface Evolution, Cambridge University Press, 2004, https://doi.org/10.1017/ CB09780511754715.
- [34] A.M. Engwall, S.J. Shin, J. Bae, Y.M. Wang, Enhanced properties of tungsten films by high-power impulse magnetron sputtering, surf, Coat. Technol. 363 (2019) 191–197, https://doi.org/10.1016/j.surfcoat.2019.02.055.
- [35] L.A. Giannuzzi, F.A. Stevie, A review of focused ion beam milling techniques for TEM specimen preparation, Micron. 30 (1999) 197–204, https://doi.org/10.1016/ S0968-4328(99)00005-0.
- [36] A. Fillon, G. Abadias, A. Michel, C. Jaouen, Stress and microstructure evolution during growth of magnetron-sputtered low-mobility metal films: influence of the nucleation conditions, Thin Solid Films 519 (2010) 1655–1661, https://doi.org/ 10.1016/j.tsf.2010.07.091.
- [37] J.R. Neighbours, F.W. Bratten, C.S. Smith, The elastic constants of nickel, J. Appl. Phys. 23 (1952) 389–393, https://doi.org/10.1063/1.1702218.
- [38] E. Chason, A.M. Engwall, Relating residual stress to thin film growth processes via a kinetic model and real-time experiments, Thin Solid Films 596 (2015) 2–7, https://doi.org/10.1016/j.tsf.2015.06.061.
- [39] F. Boydens, SIMTRA user manual version 2.1.1, (2016).